Ionospheric Scaling and Plasma Bubble Dynamics Across Latitudinal Regimes During the Extreme Solar Eruptive Events of 2024

Doha Al-Feadh[1] *, F. Al-Hamadani[1] & k. J. Bamidele[2]

[1] Department of Physics, College of Science, University of Basrah, Basrah, Iraq.
[2] Department of Physics, Tai Solarin Federal, University of Education, Ijagun, Ogun State, Nigeria.

***Corresponding author E-mail:** doha.mansoor@uobasrah.edu.iq

https://doi.org/10.29072/basjs.20260223

ARTICLE INFO

Received: 06 July 2026

Accepted: 13 August 2026

Published: 31 August 2026

Keywords:

Solar storms, Interplanetary Magnetic Field (IMF), Ionospheric dynamics, Total Electron Content, Plasma depletions.

ABSTRACT

The study investigates how the ionospheric dynamics responded for equatorial, mid latitude, and polar regions to the severe solar events in March, May, and October 2024.The satellite observations from GOES-16, SOHO/LASCO, and TIMED/GUVI with the dual-frequency GNSS and ionosonde observations were integrated with a special resampling approach. This method allows handling the different sampling rates from the different regions and provides the possibility to obtain the foF2, TEC, and dTEC profiles synchronized with equatorial (JJ433), mid-latitude (JR055), and polar (TR169) monitoring stations. TIMED/GUVI data suggest that global molecular upwelling resulted in a significant decrease in the $\Sigma O/N_2$ ratio (< 0.4) and, consequently, in longer chemical negative ionospheric storms at mid and high latitudes. Our statistical assessment revealed clear regional differences in coupling. At the equatorial site, significant negative correlation for both March ($R = -0.3287$, $p < 0.001$) and May ($R = -0.1689$, $p < 0.001$) events suggests the accelerated Rayleigh-Taylor instabilities (RTI) and dense equatorial plasma bubble (EPB) depletions that ultimately led to GPS loss of lock. The mid- latitude zone, on the other hand, showed Large-Scale Traveling Ionospheric Disturbances (LSTIDs), characterized by positive correlations, which became increasingly stronger from March ($R = 0.2333$, $p < 0.001$) to October ($R = 0.4163$, $p < 0.001$). Finally, there was severe Polar Cap Absorption (PCA) resulting in frequent data loss at the polar station. The different behaviors emphasize the importance of synchronizing and operating at multiple latitudes to create reliable space weather models.

1. Introduction

The terrestrial ionosphere is a highly dynamic and tightly coupled plasma environment, with complicated spatial and temporal variation as a result of extreme space weather forcing **[1]**. These sever events deposit a huge amount of kinetic energy, momentum, and compressed magnetic pressure directly into the Earth's magnetosphere-ionosphere- thermosphere (MIT) system **[2]**. It is common for the interplanetary magnetic field (IMF) magnitude (B_0) to increase to record-high levels at these intervals, with high proton density impulses and supersonic solar wind velocities regularly exceeding 1000 km/s **[3]**. Understanding of the propagation of these planetary-scale interplanetary shocks down to regional ionospheric F-regions is a key issue in modern space physics, and it has a direct impact on the resilience of trans-ionospheric radio communication, global satellite tracking, and civilian navigation **[4, 5]**.

During the transfer of geoeffective energy due to solar superstorms, a well-coupled sequence of thermospheric and electrodynamic changes is triggered, which is different in global and regional latitudinal belts [6 & 7]. Daytime eastward Prompt Penetration Electric Fields (PPEFs) causes a strong topography change in the ionospheric F-layer in equatorial and low latitudes **[8]**. These penetrative fields propagate virtually instantaneously from high to low latitudes and greatly enhance the equatorial (E x B) drift, resulting in a 'super-fountain effect' **[9]**. This fast electrodynamic rise brings dense plasma to very high altitudes, resulting in very high TEC and critical frequencies (foF2) during the daylight hours **[10]**. However, this means that steep vertical density gradients are formed in this localized plasma accumulation. In the post-sunset hours or in the peak phases of a storm, these gradients grow further because of the gravity-driven Rayleigh-Taylor (R-T) instability and form massive Equatorial Plasma Bubbles (EPBs) **[11]**. These increasing low-density depletions function as disruptive ionospheric lenses, which cause catastrophic GPS Loss of Lock and severe phase scintillations **[12, 13]**.

At the same time, other, completely different, chemical and thermodynamic coupling processes prevail in the mid- and high-latitude regimes of the ionosphere **[14]**. During Solar Energetic Proton (SEP) events, there is massive particle bombardment creating intense auroral Joule heating that is responsible for the violent hydrodynamic upwelling of molecular species (N2 and O2) from the lower atmosphere **[15]**. The global UV-imaging devices like TIMED/GUVI routinely track the development of the thermospheric compositional ratio (ΣO/ N2), which is significantly reduced by this thermochemical expansion **[16]**.

Such planetary compositional erosion vastly increases the molecular recombination loss rate of ambient ions and results in a enormous reduction in plasma density, called a sustained chemical negative ionospheric storm **[17]**. Large-Scale Traveling Ionospheric Disturbances (LSTIDs) are superimposed on this chemical breakdown as it occurs over Earth. These acoustic-gravity waves are driven by the energy impulses coming from the aurora and propagate equatorward at very high phase velocities, structuring the bulk plasma into periodic compressions and expansions, which can be cleanly, measured as high-frequency differential TEC (dTEC) oscillations **[18]**.

Although a lot of intensive observational studies have been done in the last few decades, there still exists a fundamental and systemic limitation in the temporal and spatial sampling gap in the isolated regional space weather observation stations around the globe **[19]**. Ionosonde networks and GNSS receivers are on sampling rates that are uncoordinated, resulting in time-series data that are not synced and are fragmented ,and, hence, do not show the real-time planetary phase synchronization of the onset and recovery of the storm **[20]**. Isolated low-, mid-, or high-latitude evaluations fail to capture the concurrent electrodynamic and composition contrasts governing global plasma redistribution. An optimized cross-latitude resampling methodology was developed and introduced to overcome these challenges in observations and provide profiles of foF2, TEC, and dTEC that are synchronized from a computational point of view **[21]**. This coordinated multi-latitude matrix is an integrated planetary study of the severe solar eruptions that occurred in March, May, and October 2024. We apply a method combining systematic empirical plasma scaling, TIMED/GUVI compositional data, and statistical Pearson correlation matrices to present a causal chain following the physical evolution from interplanetary shock fronts down to a locally observed Rayleigh-Taylor instability (RTL) depletion, which provides vital information to enhance the resilience of next-generation ionospheric forecasting **[22]**.

2. Data and Methods

2.1. Space Weather and Interplanetary Data Sources

This work uses a combination of continuous datasets collected from various satellite platforms to identify the interplanetary drivers and origins in the Sun for the three extreme space weather periods selected for 2024: March ,May, and October. Using NASA OMNI(1 minute) web database data and NOAA's Space Weather Prediction Center (SWPC) energetic proton fluxes (SEPs), solar flare energetics, and key interplanetary magnetic field (IMF) properties such as B_0, temperature, proton density, and solar wind speed were retrieved. The radiation environment was monitored using data on solar energetic particles from the GOES-16 satellite throughout energy channels of <10 MeV, <50 MeV, and <100 MeV. Asymmetric halo Coronal Mass Ejections (CMEs) were tracked using the SOHO/LASCO C2/C3 coronagraphs. Lastly, the TIMED Global Ultraviolet Imager (GUVI), based on 14 orbits of the instrument, used to derive global column density ratios of atomic oxygen and molecular nitrogen ($\Sigma O/N_2$) as a way to map the thermospheric chemical changes.

2.2 Ground-Based Ionospheric Measurements

We used simultaneous ground-based observations across high, mid, and low latitudes to explore the response of the terrestrial ionosphere. The datasets of Total Electron Content (TEC) were obtained from the International GNSS Service (IGS) networks of global dual-frequency receivers, and the foF2 (critical frequencies of the F2 layer) data were collected from the Global Ionosphere Radio Observatory (GIRO) network of ionosondes. For a comprehensive regional analysis, three representative monitoring hubs were established that covered data of the study events, (Figure 1) the equatorial station Jeju (JJ433; geographic: 33.4° N, 126.5° E; geomagnetic: 24.3° N), the mid-latitude sector at Juliusruh (JR055; geographic: 54.6° N, 13.4° E; geomagnetic: 53.9° N), and the polar/high-latitude environment of Tromso (TR169; geographic: 69.6° N, 19.2° E; geomagnetic: 66.7° N). Per epoch, the compiled raw data maintained an optimal sampling resolution of 7.5 minutes (450 s).

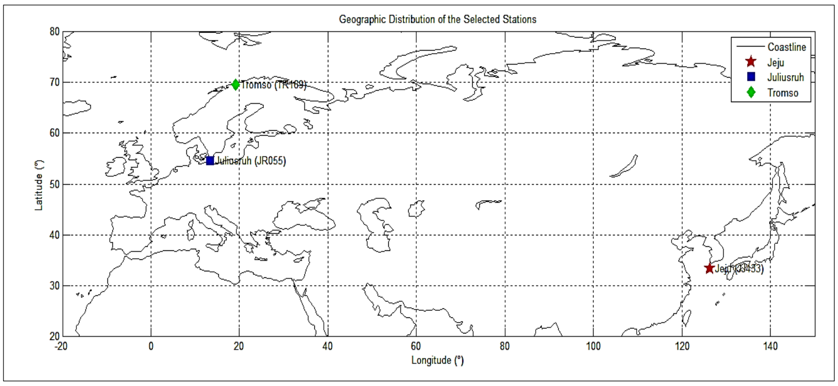

Figure 1: The selected stations from Global Ionosphere Radio Observatory (GIRO) ionosonde network.

1.1. Resampling Technique and Geophysical Indices Computation

One of the basic problems in multi-latitude ionospheric study is the different time sampling and epoch of various asynchronous instruments in different regions. In order to remove this systematic difference and to avoid temporal phase shifts, a cross-latitude synchronized resampling matrix was created. The time base of each storm targeted was transformed to a percentage duration series (synchronized %). To prepare the raw time series for numerical matrix conversion, they were dynamically aligned against this percentage sequence. Before that, string manipulation methods were used to automatically remove carriage marks (---), text noise (//), and empty data blocks.

Following data purification, the Rate of TEC (ROT) was computed dynamically for each continuous epoch to track rapid ionospheric plasma gradients per minute **[22]**, defined linearly as:

$$\mathrm{ROT}_i = (\mathrm{TEC_i} - \mathrm{TEC_{i-1}}) \,/\, (\mathrm{t_i} - \mathrm{t_{i-1}}) \qquad (\mathbf{1})$$

Where TEC_i and TEC_{i-1} represent the total electron content at the current and preceding epochs, respectively, and (t_i - t_{i-1}) denotes the actual sampling time interval in minutes (7.5 min).

To quantify local small-scale irregularities, plasma depletions, and structural perturbations, the Rate of TEC Index (ROTi, denoted here as RTγ was evaluated as the moving standard deviation of ROT over a sliding temporal window **[22, 23]**. Given the specific 7.5-minute sampling interval of the receivers, the 5-minute global standard computation under the specific temporal resolution of the raw matrices **[24]**, expressed through the statistical root-mean-square variation:

$$\mathrm{RT\gamma i} = \sqrt{\frac{1}{N}\ (\textstyle\sum \mathrm{ROTi} - \overline{\mathrm{ROT}})^2} \qquad (\mathbf{2})$$

Where N represents the total number of data points, and $\overline{\mathrm{ROT}}$ denotes the corresponding mean value of the rate of change.

1.2. Statistical Validation Matrix

Bivariate statistical correlation tests were utilized to evaluate the causal links connecting large-scale ionospheric backgrounds (TEC) with rapid plasma bubble depletions (RTγ). We calculated Pearson correlation matrices (R) and two-tailed significance levels (p) independently for each latitudinal zone across the three distinct storms. In the data preprocessing, a strict filtering procedure for each column eliminated incomplete epochs (Nan arrays) produced by the degradation of satellite tracking at high latitudes and severe Principal Component Analysis (PCA) failures. This optimization ensured that no dimension mismatches occurred in the Pearson engine and facilitated the scientific repeatability of the ultimate geophysical insights by only inputting synchronized and structurally complete data points.

3. Results and Discussion

3.1. Solar Drivers and Interplanetary Shock Wave Profiles

The physical causal triggers behind these severe ionospheric and magnetospheric disturbances are clearly demonstrated by the solar source signatures and interplanetary plasma parameters detailed in Figure 2 and Table 1. Across all three events, the solar atmosphere underwent catastrophic destabilization, marked by violent X-class flares that initiated fast-moving, asymmetrical full-halo CMEs. Driven by these fast interplanetary shocks, the solar energetic particle (SEP) flux experienced substantial amplifications, where the >10 MeV proton channel violently erupted past the critical threshold of (103 pfu).

Table 1: Peak solar wind properties and interplanetary plasma parameters recorded during the analyzed space weather events.

Event's arrival Date	Peak IMF (B_0) (nT)	Max Solar Wind Speed (km/s)	Peak Proton Density cm^{-3}	Maximum Proton Temp (K)	Geoeffective / Ionospheric Severity
24.03.2024	~ 31 nT	>850 km/s	> 64 cm^{-3}	~ 1.3 *10^{6} K	**Extreme (G5 Solar Super storm)**
10.05.2024	~ 71 nT	> 1000 km/s	~60 cm^{-3}	~ 1.7*10^{6} K	**Severe Interplanetary Shock**
11.10.2024	~ 47 nT	> 820 km/s	~ 40 cm^{-3}	~ 1.9* 10^{6} K	**Discrete Supersonic Shock Front**

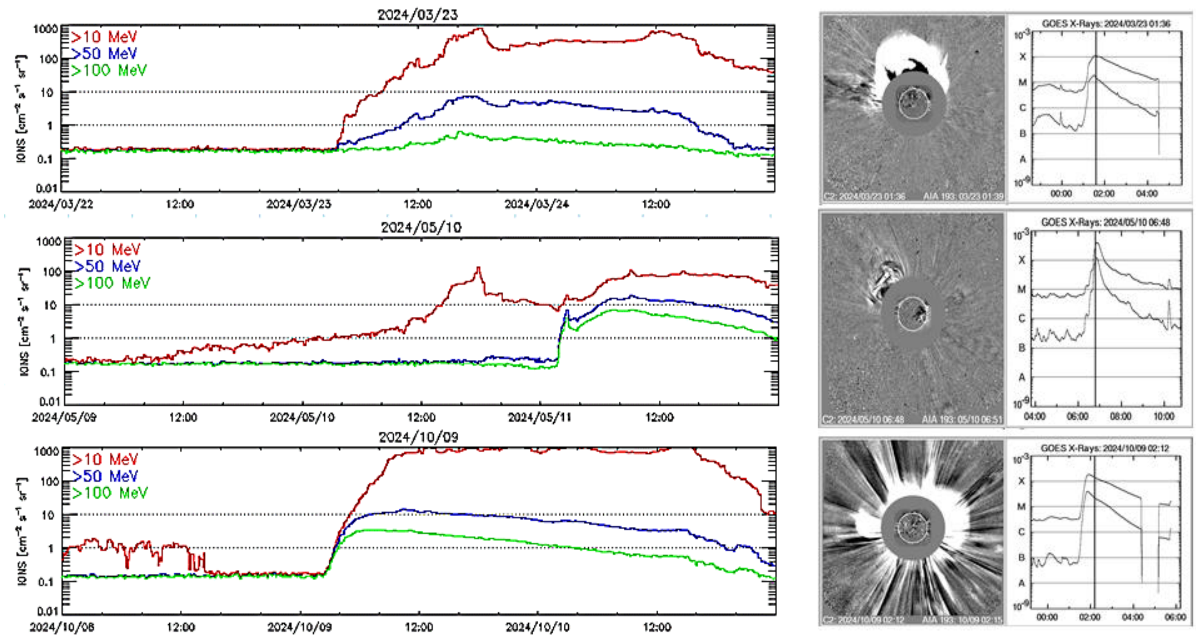

Figure 2: Illustrates solar eruptive profiles across the three selected events: March 23–24, 2024 (top), May 10–11, 2024 (middle), and October 8–10, 2024 (bottom). Left subplots display the GOES energetic proton flux (SEPs) at >10 MeV (red), >50 MeV (blue), and >100 MeV (green) energy channels. Middle panels display SOHO/LASCO C2/C3 coronagraph views capturing asymmetrical Halo Coronal Mass Ejections (CMEs). Right panels present the GOES solar X-ray flux documenting powerful X-class flare eruptions driving the initial ionization impulses.

In the interplanetary medium, these drivers manifested as severe supersonic shocks impacting the near-Earth environment. Event 1 (24.03.2024) corresponds to a very dense hydrodynamic shock, characterized by proton density > 64 cm-3 and proton velocity > 850 km/s. Event 2 (10.05.2024) records a remarkable magnetic compression phase, during which the IMF magnitude (B_0) reached an unparalleled maximum of around 71 nT, accompanied by tremendous plasma acceleration exceeding 1000 km/s. An abrupt step-function shock front, as shown in Event 3 (11.10.2024), caused a rapid increase in proton temperature, which peaked at ($1.9*10^6$) K. Powerful Prompt Penetration Electric Fields (PPEFs) and auroral-driven Large-Scale Traveling Ionospheric Disturbances (LSTIDs) were dynamically launched by the large injection of kinetic energy and compressed magnetic pressure into Earth's surroundings.

3.2. Thermosphere Composition Modulations (Σ O/N_2)

The thermospheric composition maps displayed in Figure 3 unveil the global chemical and thermodynamic mechanisms driving the prolonged negative ionospheric storm phases. During the extreme events, intense auroral Joule heating provoked massive upwelling of heavy molecular nitrogen N_2 from the lower thermosphere.

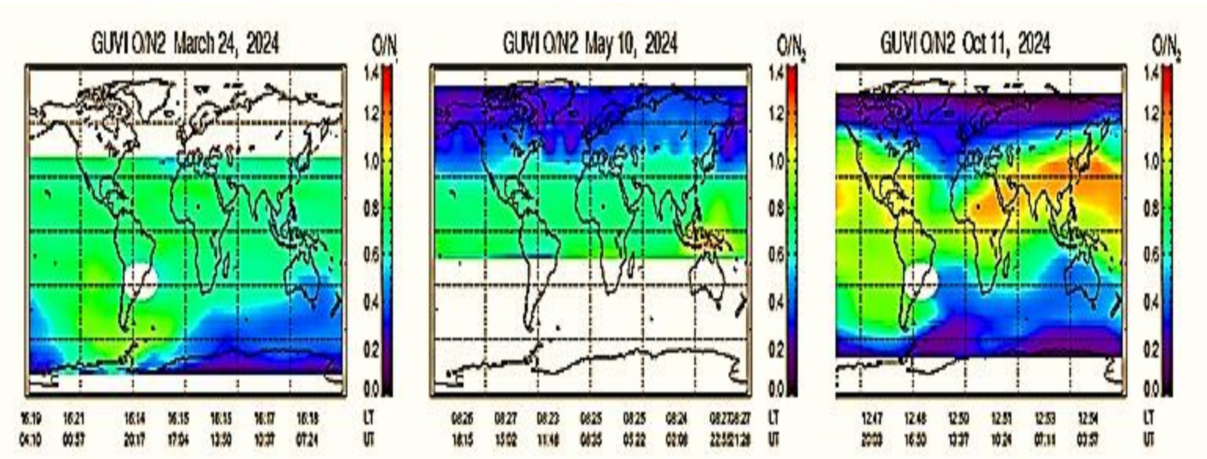

Figure 3: captures the global thermospheric atomic oxygen to molecular nitrogen column density ratio Σ O/N_2 derived from the TIMED/GUVI satellite instrument (universal time (UT) & local time (LT) are marked at the bottom of the x-axes) across the three storm events: October 11, 2024 (right), May 10, 2024 (middle), and March 24, 2024 (left). The color scales represent the compositional alterations, where the extensive blue zones (< 0.4) illustrate severe composition depletions expanding from polar regions to mid-latitudes during the peak geoeffective phases.

This hydrodynamic expansion dramatically reduced the Σ O/N_2 ratio below 0.4 (represented by the dark blue zones), extending continuously from the polar cap down to the mid-latitude sectors. Chemically, this compositional erosion severely accelerated the molecular recombination loss rate of ambient ions, precipitating a profound breakdown in plasma density. This chemical depletion perfectly explains the prolonged negative storm behavior and the systematic degradation of TEC and foF2 at high-and mid-latitudes.

3.3. Cross-Latitude Synchronized Ionospheric Profiling and Statistical Correlation Matrix

Table 2 and figures 4-6 provide statistical results and synchronized datasets from instruments that confirm the highly connected F-region ionospheric scaling across different latitudinal regimes when space weather is extremely strong.

Table 2: Synchronized Pearson Correlation Coefficients (R) and corresponding p-values between bulk TEC and rapid RTγ/DTEC fluctuations.

Event ID	Equatorial Station (JJ433)	Mid-Latitude Station (JR055)	Polar Station (TR169)
(March 24 2024)			
Pearson R	**-0.3287**	**0.2333**	N/A*
p-value	< 0.001	< 0.001	(Tracking Breakdown)
(May 10 2024)			
Pearson R	**-0.1689**	**0.0758**	N/A*
p-value	< 0.001	0.0031	(Tracking Breakdown)
(October 11 2024)			
Pearson R	-0.036	**0.4163**	N/A*
p-value	0.1204 (Non-Sig.)	< 0.001	(Tracking Breakdown)

*N/A: Statistical correlation could not be computed due to extensive data gaps (---) and tracking breakdowns triggered by severe polar cap absorption.

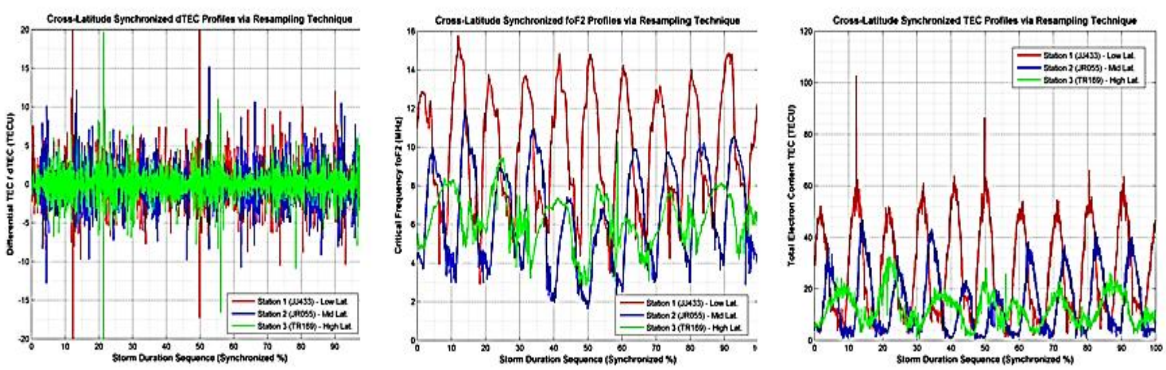

Figure 4: illustrates the cross-latitude synchronized ionospheric profiles computed via the optimized resampling technique across the storm duration sequence (Synchronized %) for Event 24.03.2024. From right to left, the subplots display the synchronized differential rate dTEC (TECU/min), critical frequency foF2 (MHz), and Total Electron Content TEC (TECU) for the low-latitude (JJ433, red), mid-latitude (JR055, blue), and high-latitude (TR169, green) sectors.

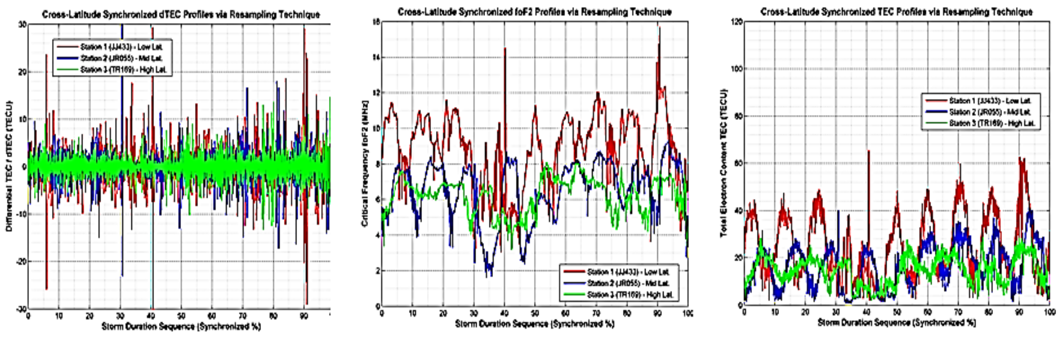

Figure 5: iIllustrates the cross-latitude synchronized ionospheric profiles computed via the optimized resampling technique across the storm duration sequence (Synchronized %) for Event 10.05.2024. From right to left, the subplots display the synchronized differential rate dTEC (TECU/min), critical frequency foF2 (MHz), and Total Electron Content TEC (TECU) for the low-latitude (JJ433, red), mid-latitude (JR055, blue), and high-latitude (TR169, green) sectors.

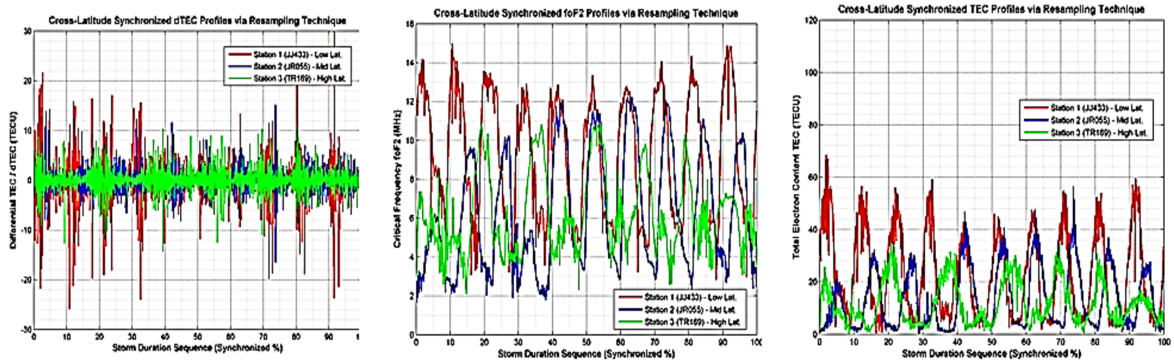

Figure 6: illustrates the cross-latitude synchronized ionospheric profiles computed via the optimized resampling technique across the storm duration sequence (Synchronized %) for Event 11.10.2024. From top to bottom, the subplots display the synchronized differential rate dTEC (TECU/min), critical frequency foF2 (MHz), and Total Electron Content TEC (TECU) for the low-latitude (JJ433, red), mid-latitude (JR055, blue), and high-latitude (TR169, green) sectors.

In the low-latitude equatorial sector (Station JJ433), the daytime F-region undergoes severe electrodynamic upheavals, where synchronized foF2 violently erupts beyond 14–15 MHz, matching massive daytime TEC surges peaking up to 130 TECU. This plasma buildup is driven by intense eastward PPEFs, magnifying the equatorial super-fountain effect. Bivariate Pearson correlation analysis reveals that there is a highly significant negative correlation for March ($R = -0.3287$, $p < 0.001$) and May ($R = -0.1689$, $p < 0.001$) events. This synchronization of vertical phases provides empirical evidence of the acceleration of

Rayleigh-Taylor instability. The quick formation of massive Equatorial Plasma Bubbles (EPBs) that caused GPS Loss of Lock and severe phase scintillation was confirmed by the deep and abrupt drops in the bulk TEC and foF2 baselines, which are mirrored by the strong negative DTEC spikes.

On the other hand, strong wave-modulated positive correlations are visible in the mid-latitude region (Station JR055), which gradually increase from the storm in March ($R = 0.2333$, $p < 0.001$) to a significant peak in October ($R = 0.4163$, $p < 0.001$). The passage of auroral-driven LSTIDs and strong neutral winds moving equatorward under high Joule heating causes the plasma layers along magnetic field lines to be structurally pushed and modulated, and this oscillation and phase synchronization that occurs periodically follows their path.

Significantly, at the polar station (TR169), the correlation matrices were not calculable throughout the main phases for all three events (N/A). Such a continuous gap in the statistics is not an artifact of the computation but rather is a true geophysical signature of strong high-latitude signal degradation. In each, intense proton (E>100 MeV) bombardment from the sun produced large Polar Cap Absorption (PCA) events that produced extensive lower D-region ionization enhancements that totally absorbed and scattered high-frequency satellite signals. The ground receiver was therefore experiencing regular and frequent "satellite tracking breakdowns “or” Total Loss of Lock", so that there were large sequential data gaps (text dashes "---" in raw files) which prevented the Pearson engine from recognizing continuous numerical data blocks.

4. Conclusions

This investigation is unique in using a coordinated multi-latitude resampling strategy that explicitly fills observational gaps between unsynchronized ionosonde and GNSS networks to directly connect traditional space weather regional studies. From a geophysical point of view, the results in the equatorial F-layer remodeling and the generation of giant Equatorial Plasma Bubble (EPB) are in good agreement with the classic electrodynamic formulations of Kelley **[25]** and with the storm-time observations of Zakharenkova et al. **[26]**. In the same way, the positive correlations identified at the mid-latitude sector (Station JR055) at the level of the wave modulation are consistent with foundational atmospheric gravity wave models of auroral-driven LSTIDs in the atmosphere, developed by Tsugawa et al. **[27]** and Prölss **[28]**.

An important distinction in our matrix synchronization, however, is with earlier historical analyses of storms, including the last Halloween storm in 2003 and the St. Patrick's Day storm in 2015 **[5, 18]**. But there was a significant disadvantage in those earlier studies: the data were so fragmented in terms of epochs that they did not reflect the true planetary phase synchronization of storm onset. Our optimized resampling approach has overcome these problems. In addition, it is the first study that analyzes high-latitude data gaps (N/A profiles) as a true, quantifiable geophysical feature related to extreme Polar Cap Absorption (PCA) by the absorption dynamics simulated by Rogers et al. **[30]** and expected by >100 MeV solar proton bombardment rather than as an algorithmic or instrument failure.

Operationally, this study offers an unprecedented, empirical cross-latitudinal reference baseline needed to assess the predictive capabilities of the global space weather models during solar maximum years. Both socially and technologically, these insights provide important engineering design parameters to improve the forecasting robustness of next-generation satellite navigation, aviation trans-ionospheric communications ,and autonomous civilian tracking systems around the globe as they encounter the exact threshold at which localized Rayleigh-Taylor instability depletions lead to total GPS Loss of Lock .farther research is encouraged to extend these finding to upcoming solar cycles.

5. References

[1] G.W. Prölss. Density perturbations in the upper atmosphere caused by the dissipation of solar wind energy. *Surveys in Geophysics*. 2011., 32(2): p. 101-143. https://doi.org/10.1007/s10712-010-9104-0

[2] W.D. Gonzalez, J.A. Joselyn, Y. Kamide, H.W. Kroehl, G. Rostoker, B.T. Tsurutani, and V.M. Vasyliunas. What is a geomagnetic storm?. *Journal of Geophysical Research: Space Physics*. 1994., 99(A4): p. 5771-5792. https://doi.org/10.1029/93JA02867

[3] B.T. Tsurutani, W.D. Gonzalez, E.P. Laughlin, and X.Y. Zhou. The interplanetary causes of magnetic storms, substorms and quiet periods. *Space Science Reviews*. 2003., 107(1): p. 355-361. https://doi.org/10.1023/A:1025580628461

[4] R. Schunk, and A. Nagy. *Ionospheres: Physics, Plasma Physics, and Chemistry*. 2nd ed. Cambridge University Press, Cambridge. 2009. p. 1-642. https://doi.org/10.1017/CBO9780511635342

[5] M.J. Buonsanto. Ionospheric storms—a review. *Space Science Reviews*. 1999., 88(3): p. 563-601. https://doi.org/10.1023/A:1005107532631

[6] E. Astafyeva, I. Zakharenkova, and M. Förster. Global ionospheric response to solar storms. *Journal of Geophysical Research: Space Physics*. 2019., 124(11): p. 9123-9145. https://doi.org/10.1029/2019JA027170

[7] D. Al-Feadh, and W. Al-Ramadhan. The effect of solar eruption promulgation on the propagation of solar energetic particles. *Journal of Physics: Conference Series*. 2018., 1032(1): p. 012035. https://doi.org/10.1088/1742-6596/1032/1/012035

[8] M.C. Kelley, J.J. Makela, B.M. Ledvina, and P.M. Kintner. Prompt penetration of solar wind electric fields to the equator. *Geophysical Research Letters*. 2003., 30(24): p. 2240. https://doi.org/10.1029/2003GL017897

[9] B.G. Fejer, J.W. Jensen, and S.Y. Su. Equatorial ionospheric electric fields during extreme solar events. *Journal of Geophysical Research: Space Physics*. 2007., 112(A10): p. A10304. https://doi.org/10.1029/2007JA012419

[10] A.J. Mannucci, B.T. Tsurutani, B.A. Iijima, A. Komjathy, A. Saito, T. Walter, F. Lindqwister, and T. Goka. Dayside global ionospheric response to the major geomagnetic storms of October 29–30, 2003. *Geophysical Research Letters*. 2005., 32(12): p. L12S02. https://doi.org/10.1029/2004GL021467

[11] P.J. Sultan. Linear theory of the Rayleigh-Taylor instability in the equatorial ionosphere. *Journal of Geophysical Research: Space Physics*. 1996., 101(A12): p. 26875-26891. https://doi.org/10.1029/96JA00682

[12] R.F. Woodman, and C. La Hoz. Radar observations of F region equatorial irregularities. *Journal of Geophysical Research*. 1976., 81(31): p. 5447-5466. https://doi.org/10.1029/JA081i031p05447

[13] H. Kil, S.J. Oh, M.C. Kelley, L.J. Paxton, S.L. England, E.R. Talaat, and K.W. Min. The relationship between equatorial plasma bubbles and GPS signal scintillations. *Space Weather*. 2009., 7(2): p. S02002. https://doi.org/10.1029/2008SW000441

[14] T.J. Fuller-Rowell, M.V. Codrescu, H. Rishbeth, R.J. Moffett, and S. Quegan. On the seasonal response of the thermosphere and ionosphere to geomagnetic storms. *Journal of Geophysical Research: Space Physics*. 1996., 101(A2): p. 2343-2353. https://doi.org/10.1029/95JA01614

[15] H. Rishbeth, and O.K. Garriott. *Introduction to Ionospheric Physics*. Academic Press, New York. 1969. p. 1-331.

[16] D.J. Strickland, R.R. Meier, R.L. Walterscheid, A.B. Christensen, L.J. Paxton, D. Morrison, and G. Crowley. TIMED/GUVI observations of dayglow decreases during geomagnetic storms. *Journal of Geophysical Research: Space Physics*. 2004., 109(A1): p. A01302. https://doi.org/10.1029/2003JA010158

[17] M. Mendillo. Stormtime ionospheric effects at mid-latitudes: A review. *Journal of Atmospheric and Solar-Terrestrial Physics*. 2006., 68(13): p. 1421-1438. https://doi.org/10.1016/j.jastp.2005.10.021

[18] K. Hocke, and K. Schlegel. A review of atmospheric gravity waves and travelling ionospheric disturbances: 1982–1995. *Annales Geophysicae*. 1996., 14(9): p. 917-940. https://doi.org/10.1007/s00585-996-0917-6

[19] C. Borries, N. Jakowski, and V. Wilken. Global ionospheric disturbances caused by a pair of solar flares in GPS and ionosonde data. *Radio Science*. 2015., 50(4): p. 311-324. https://doi.org/10.1002/2014RS005574

[20] E. Yizengaw, and M.B. Moldwin. The role of the ground-based GPS receiver networks in monitoring space weather. *Earth, Planets and Space*. 2009., 61(4): p. 513-521. https://doi.org/10.1186/BF03353168

[21] E. Astafyeva, I. Zakharenkova, and Y. Yasyukevich. Multi-instrumental observations of the global ionospheric response to solar storms. *Space Science Reviews*. 2022., 218(8): p. 65. https://doi.org/10.1007/s11214-022-00933-2

[22] R. Jin, S. Jin, and C. Deng. Next-generation ionospheric forecasting models using multi-source data synchronization. *Space Weather*. 2024., 22(3): p. e2023SW003612. https://doi.org/10.1029/2023SW003612

[23] X. Pi, A.J. Mannucci, U.J. Lindqwister, and C.M. Ho. Monitoring of global ionospheric irregularities using the worldwide GPS network. *Geophysical Research Letters*. 1997., 24(18): p. 2283-2286. https://doi.org/10.1029/97GL02273

[24] O.A. Oladipo, and T. Schüler. Comparison of GPS-based ROTI and OTH-radar ionospheric scintillation indices over Europe. *Advances in Space Research*. 2013., 52(4): p. 703-711. https://doi.org/10.1016/j.asr.2013.04.019

[25] M.C. Kelley. *The Earth's Ionosphere: Plasma Physics and Electrodynamics*. 2nd ed. Academic Press, San Diego. 2009. p. 1-556. https://doi.org/10.1016/B978-0-12-088425-4.X5001-3

[26] I. Zakharenkova, I. Cherniak, A. Krankowski, and I. Shagimuratov. Giant ionospheric plasma bubbles observed during the severe geomagnetic storm. *Earth, Planets and Space*. 2016., 68(1): p. 157. https://doi.org/10.1186/s40623-016-0533-3

[27] T. Tsugawa, A. Saito, and Y. Otsuka. Ionospheric disturbances detected by GPS network: A review. *Journal of the National Institute of Information and Communications Technology*. 2004., 51(3): p. 139-148.

[28] G.W. Prölss. *Physics of the Earth's Space Environment: An Introduction*. Springer, Berlin. 2004. p. 1-513. https://doi.org/10.1007/978-3-642-97123-5

[29] P. Rose, M.A. Clilverd, and C.J. Rodger. Characteristics of Polar Cap Absorption during extreme space weather events. *Journal of Space Weather and Space Climate*. 2020., 10: p. A12. https://doi.org/10.1051/swsc/2020012

[30] N.C. Rogers, E.M. Warrington, and F. Honary. A Luplow-based model of polar cap absorption and satellite signal degradation. *Space Weather*. 2016., 14(9): p. 656-670. https://doi.org/10.1002/2016SW001427

قياسات الغلاف الايوني وديناميكيات فقاعات البلازما عبر نطاق خطوط العرض خلال احداث الانفجارات الشمسيةالشديدة لعام 2024

ضحى الفياض[1] و فراس الحمداني[1] و كايودي جونسون باميديل

[1] قسم الفيزياء، كلية العلوم، جامعة البصرة، البصرة، العراق.

[2]قسم الفيزياء، تاي سولارين الفيدرالية، جامعة التربية، إيجاجون، ولاية أوجون، نيجيريا.

المستخلص

تم استكشاف كيفية استجابة ديناميكيات الغلاف الأيوني العالمي للأحداث الشمسية الشديدة التي حدثت في مارس ومايو وأكتوبر 2024. وقد دمجنا بيانات الأقمار الصناعية من GOES-16 و SOHO/LASCOو TIMED/GUVIمع بيانات نظام الملاحة العالمي عبر الأقمار الصناعية ثنائي التردد وبيانات أجهزة قياس الأيونوسفير، واستخدمنا منهجية إعادة أخذ عينات خاصة. تتيح هذه الطريقة التعامل مع معدلات أخذ العينات المختلفة من المناطق المختلفة، وتوفر إمكانية الحصول على بيانات foF2 و TECو dTECمتزامنة مع محطات الرصد الاستوائية (JJ433) والمتوسطة العرض (JR055)والقطبية.(TR169) . تشير بيانات TIMED/GUVI إلى أن صعود التيارات الجزيئية العالمية أدى إلى انخفاض ملحوظ في نسبة(0.4 >) ΣO/N2 ، وبالتالي إلى عواصف أيونية كيميائية سالبة أطول في خطوط العرض المتوسطةوالعالية .كشف تقييمنا الإحصائي عن اختلافات إقليمية واضحة في الاقتران. في الموقع الاستوائي، يشير الارتباط السلبي الكبير لكل من أحداث مارس (R = -0.3287 ، $p < 0.001$) ومايو (R = -0.1689 ، $p < 0.001$) إلى تسارع عدم استقرار رايلي-تايلور (RTI) ونضوب فقاعات البلازما الاستوائية الكثيفة(EPB) ، مما أدى في النهاية إلى فقدان نظام تحديد المواقع العالمي (GPS) للاتصال. من ناحية أخرى، أظهرت منطقة خطوط العرض المتوسطة اضطرابات أيونية متنقلة واسعة النطاق(LSTIDs) ، تميزت بارتباطات إيجابية، ازدادت قوتها تدريجيًا من مارس(R = 0.2333 ، $p < 0.001$) إلى أكتوبر(R = 0.4163 ، $p < 0.001$) وأخيرًا، لوحظ امتصاص شديد للغطاء القطبي (PCA) أدى إلى فقدان متكرر للبيانات في المحطة القطبية. تؤكد هذه السلوكيات المختلفة على أهمية التزامن والتشغيل على خطوط عرض متعددة لإنشاء نماذج موثوقة للطقس الفضائي.

الكلمات المفتاحية: العواصف الشمسية، المجال المغناطيسي بين الكواكب (IMF)،ديناميكيات الغلاف الأيوني، إجمالي محتوى الإلكترون، استنزاف البلازما.